RSC Advances




ROYAL SOCIETY OF CHEMISTRY

www.rsc.org/advances

Journal Name

ARTICLE

# Superior rate performance of $Li_3V_2(PO_4)_3$ co-modified by Fe-doping and rGO-incorporating

Received 00th January 20xx,
Accepted 00th January 20xx

DOI: 10.1039/x0xx00000x

www.rsc.org/

Zhen Li[a], Lu-Lu Zhang[a,b*], Xue-Lin Yang[a*], Hua-Bin Sun[a], Yun-Hui Huang[c] and Gan Liang[d]

The reduced graphene oxide (rGO) incorporated $Li_3V_{1.94}Fe_{0.06}(PO_4)_3$/C cathode materials were successfully prepared by sol-gel method. Compared with $Li_3V_2(PO_4)_3$/C and single rGO-incorporated $Li_3V_2(PO_4)_3$/C, the rGO-incorporated $Li_3V_{1.94}Fe_{0.06}(PO_4)_3$/C electrode behaves the highest initial capacity of 164.4 mAh $g^{-1}$ with a capacity retention ratio of 83.5 % after 100 cycles at 1 C. When charged/discharged 1000 cycles at 5 C, it exhibits a prominent capacity of 129.3 mAh $g^{-1}$ with a capacity retention ratio of 91.5 % and a very low capacity fading of 0.0085 % per cycle. The superior electrochemical performance of Fe-doped and rGO-incorporated $Li_3V_2(PO_4)_3$ can be contributed to the reduced particle size, the improved electronic conductivity, and the increased Li-ion diffusion coefficient. We believe this novel co-modification with Fe-doping and rGO-incorporating is an efficient way for $Li_3V_2(PO_4)_3$ and any other polyanion cathode materials to realize their application in power lithium ion battery.

## 1. Introduction

Common power lithium ion battery cathode materials are lithium cobalt oxide, spinel lithium manganate, nickel cobalt manganese ternary material, and polyanion cathode materials ($LiMPO_4$, M = Mn, Fe and V, etc.)[1-4]. Among them, polyanion cathode materials are the subject of more extensive research and development because of their high safety, especially monoclinic $Li_3V_2(PO_4)_3$ (LVP)[5]. In LVP, the $Li^+$ ions are inserted or extracted through the host framework of $V_2(PO_4)_3$, which consists of the slightly distorted $VO_6$ octahedra and $PO_4$ tetrahedra sharing the oxygen vertices [6-8]. All three $Li^+$ ions in LVP are extractable at room temperature, leading to the highest theoretical capacity (197 mAh $g^{-1}$) for any reported phosphate materials. However, the metal octahedra and phosphate tetrahedra in LVP share oxygen vertices, thus a 3D electoniclly conductive network cannot be formed and the electronic conductivity is relatively poor (about $2.3\times10^{-8}$ S $cm^{-1}$ at room temperature), which limits its higher capacity and further practical applications [4,9-11]. Much effort (carbon coating, cation doping, etc.) has been made to overcome this drawback.

Carbon coating is one of the most effective methods to improve the electronic conductivity. As we known, pyrolytic carbon from organic carbon sources (glucose, sucrose, citric acid, etc.) [12-15] and traditional inorganic carbon (carbon black, acetylene black, graphite, etc.) [16,17] have been widely used for cathode materials to improve their intrinsic electronic conductivity. Recently, graphene and reduced graphene oxide (rGO) have been reported to be used as a conductive coating material for some polyanion cathode materials, such as LFP [18], LVP [19,20], LFS [21] and so on. Compared to pyrolytic carbon and traditional inorganic carbon, graphene and rGO are monolayer carbon-atom sheet and form hexagonal honeycomb lattice structure with $sp^2$ hybrid orbital, resulting in large specific surface area, excellent electrical conductivity, and high chemical stability [22-26]. Graphene (or rGO) and the corresponding coated cathode material particles can form a 3D network structure, leading to an enhanced electronic conductivity and electrochemical properties of polyanion cathode materials [27-34]. Besides, cation doping has also been proven to be effective for enhancing the intrinsic electronic conductivity of polyanion materials [3,35,36]. Many cations, such as Co [37], Ti [38], Y [39], Mg [40], Cr [41] and Fe [42], have been reported to show positive doping effects in LVP. Our group ever systematically investigated the effect of Fe-doping on physicochemical properties and electrochemical performances of LVP. It was found that Fe-doping can significantly enhance the electrochemical performance of LVP not only due to reduced particle size and decreased charge-transfer resistance, but also due to the suppressed vanadium dissolution in electrolyte over cycling by $FePO_4$. However, there is still no report about co-modification by Fe-doping and rGO-incorporation for LVP and any other cathode materials.

[a] College of Materials and Chemical Engineering, Hubei Provincial Collaborative Innovation Center for New Energy Microgrid, China Three Gorges University, 8 Daxue Road, Yichang, Hubei 443002, China. Email: zlljoy@126.com.
[b] CAS Key Laboratory of Materials for Energy Conversion, Shanghai Institute of Ceramics, Chinese Academy of Sciences, Shanghai 200050, China
[c] School of Materials Science and Engineering, State Key Laboratory of Material Processing and Die & Mould Technology, Huazhong University of Science and Technology, 1037 Luoyu Road, Wuhan, Hubei 430074, China
[d] Department of Physics, Sam Houston State University, Huntsville, Texas 77341, USA

† Footnotes relating to the title and/or authors should appear here.
Electronic Supplementary Information (ESI) available: [details of any supplementary information available should be included here]. See DOI: 10.1039/x0xx00000x

In this work, a series of rGO-incorporated and Fe-doped LVP/C composites were successfully prepared by sol-gel method, and characterized by X-ray diffraction (XRD), Raman spectroscopy, scanning electron microscopy (SEM) and transmission electron microscopy (TEM). The common effect of Fe-doping and rGO-incorporating on electrochemical performance of LVP was also explored by galvanostatic charge/discharge, cyclic voltammetry (CV) and electrochemical impedance spectra (EIS) measurements.

## 2. Experimental

### 2.1 Synthesis of LVP/C@G

All the chemical reagents were of analytical grade and used as received without any further purification. $LiOH{\cdot}H_2O$, $NH_4VO_3$, $FeC_2O_4{\cdot}2H_2O$, $NH_4H_2PO_4$, $C_2H_2O_4{\cdot}2H_2O$ and graphene oxide (GO) were used as the raw materials. The synthesis process is as follows: first, $C_2H_2O_4{\cdot}2H_2O$ and $NH_4VO_3$ were dissolved in deionized water under stirring at 80 °C for an hour in a stoichiometric molar ratio of 3:1. Then, stoichiometric $LiOH{\cdot}H_2O$ and $NH_4H_2PO_4$ were added in turn. Subsequently, GO dispersion (the GO content is 1, 3 and 5 wt.%, respectively) was introduced into the above solution, and the mixture was stirred at 80 °C to remove the excess water and the resulting blue-black gel was dried at 120 °C for 12 h. Afterwards, the gel precursors were heated at 350 °C for 6 h under $Ar/H_2$ (5 % $H_2$) atmosphere and then cooled down to room temperature. Then different amounts of glucose were added to ensure the similar carbon content in compared samples, and milled for 2 h in ethanol. Finally, the mixture was sintered at 700 °C for 10 h under $Ar/H_2$ (5 % $H_2$) atmosphere to achieve the rGO modified LVP/C composites. These products prepared with 1, 3 and 5 wt.% GO are denoted as LVP/C@G1, LVP/C@G3 and LVP/C@G5, respectively. For comparison, another LVP/C composite was also prepared via the same process without GO, and denoted as LVP/C.

### 2.2 Synthesis of LVFP/C@G3

Figure 1 shows the synthesis procedure for the Fe-doped composites ($Li_3V_{2-x}Fe_x(PO_4)_3$/C@G3, $x$ = 0.02, 0.06 and 0.10), which is basically the same as that for the undoped samples. The difference is that $FeC_2O_4{\cdot}2H_2O$ is substituted for partial $NH_4VO_3$, and the molar ratio of $C_2H_2O_4{\cdot}2H_2O$: (V + Fe) is 3 : 1; moreover the GO content is 3 wt.%. The $Li_3V_{2-x}Fe_x(PO_4)_3$/C composites with $x$ = 0.02, 0.06 and 0.10 are denoted as LVFP/C@G3-1, LVFP/C@G3-2 and LVFP/C@G3-3, respectively.

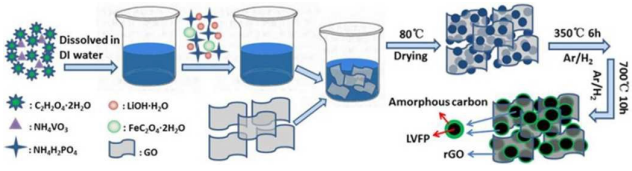


**Figure 1.** Schematic illustration of the synthesis process for $Li_3V_{2-x}Fe_x(PO_4)_3$/C@G (x = 0.02, 0.06 and 0.10) composites.

### 2.3 Sample analysis

X-ray diffraction patterns were recorded using an X-ray diffractometer (Rigaku Ultima IV) with Cu-$K_\alpha$ radiation. The structure of residual carbon in LVP/C, LVP/C@G3 and LVFP/C@G3-2 samples was verified by a Raman spectroscopy system (VERTEX 70, Bruker). The morphology of samples was obtained with a scanning electron microscope (SEM, Sirion 200, Holland).

### 2.4 Electrochemical measurements

The working electrodes were fabricated by the following mixture: 75 wt.% active material, 15 wt.% acetylene black, and 10 wt.% PVDF in N-methyl pyrrolidinone (0.02 g $mL^{-1}$) on an aluminum foil (20 μm in thickness). Electrode film was punched into discs of 14 mm diameter and was pressed under a pressure of 6 MPa. After dried at 120 °C for 10 h in vacuum, electrodes were transferred into an argon-filled glove box (Super 1220/750, Mikrouna). The 2025 coin cells were assembled using Celgard 2400 as separator, lithium foil as counter and reference electrodes, and 1 $mol{\cdot}L^{-1}$ $LiPF_6$ in a 1:1 volumetric mixture of ethylene carbonate and diethyl carbonate (EC/DEC) as electrolyte. The specific capacity was measured at constant charge/discharge current between 3.0 and 4.8 V (vs. $Li^+$/Li) on a cell test system (LAND CT2001A, China). Cyclic voltammetry (CV) curves and electrochemical impedance spectra (EIS) were obtained using an electrochemical workstation (CHI614C, China). The EIS spectra were obtained in a frequency range from 0.01 Hz to 100 kHz.

## 3. Results and discussions

Figure 2 shows the XRD patterns of LVP/C, rGO modified LVP/C composites (LVP/C@G1, LVP/C@G3 and LVP/C@G5) and Fe-doped LVP/C@G3 composites (LVFP/C@G3-1, LVFP/C@G3-2 and LVFP/C@G3-3), respectively. The main diffraction peaks of all the samples are well indexed to a monoclinic $Li_3V_2(PO_4)_3$ structure phase (JCPDS, No. 72-7074) with space group of $P2_1/n$, which indicates that low dose of Fe and rGO incorporating has no inherent effect on the lattice structure of LVP. Diffraction lines of carbon are not observed, indicating that the residual carbon is perhaps in amorphous phase or its content is too low to be detected. The carbon content of LVP/C, LVP/C@G3, and LVFP/C@G3-2 is measured to be about 1.894, 1.888, and 1.831 wt.%, respectively (Table 1).

To further investigate the structure of residual carbon in samples, Raman spectra of LVP/C, LVP/C@G3 and LVFP/C@G3-2 were collected. As shown in Figure 3, two intense broad bands around 1351 and 1577 $cm^{-1}$ are detected, which are assigned to the disordered (D) and graphite (G) bands of carbon, respectively [43]. The $I_D/I_G$ value of LVFP/C@G3-2 is about 0.74, which is lower than that of both LVP/C@G3 (1.05) and LVP/C (1.19). The decreased $I_D/I_G$ for LVFP/C@G3-2 is mainly ascribed to the catalytic effect of Fe on the

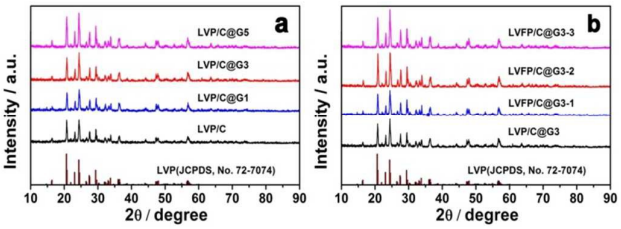


**Figure 2.** XRD patterns of the as-prepared samples.

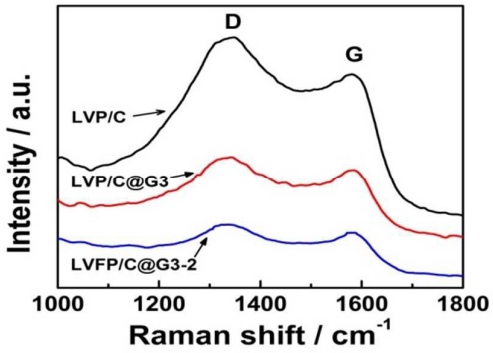


**Figure 3.** Raman spectra of LVP/C, LVP/C@G3 and LVFP/C@G3-2 composites.

**Table 1.** Carbon content, electronic conductivity and EIS parameters of samples.

| Sample | LVP/C | LVP/C@G3 | LVFP/C@G3-2 |
|---|---|---|---|
| Carbon content / % | 1.894 | 1.888 | 1.831 |
| Electronic conductivity (S $cm^{-1}$) | $0.60\times10^{-3}$ | $4.63\times10^{-3}$ | $6.62\times10^{-3}$ |
| $R_{ct}$ (Ω) | 55.66 | 32.51 | 20.57 |
| $\delta$ (Ω $cm^2$ $s^{-1/2}$) | 164.19 | 83.95 | 26.73 |
| $D_{Li+}$ ($cm^2$ $s^{-1}$) | $5.56\times10^{-13}$ | $2.13\times10^{-12}$ | $2.10\times10^{-11}$ |

graphitization of carbon [44-46]. The lower $I_D/I_G$ value means more graphite-like carbon in the residual carbon, leading to an enhanced electronic conductivity of LVFP/C@G3-2 (Table 1).

Figure 4 shows the SEM images of LVP/C, LVP/C@G3 and LVFP/C@G3-2 powders. All the samples present irregular shape and different degree of agglomeration. The average size of particles is ~1.5 μm. Compared with LVP/C, the LVP/C@G3 particles exhibit more uniform and less agglomeration (Figure 4b). The particle size distribution of LVP/C@G3 samples is between 0.5 ~ 1.5 μm. Figure 4c shows that the particle size of LVFP/C@G3-2 is smaller than that of LVP/C and LVP/C@G3. LVFP/C@G3-2 shows the smallest particle size between 0.2 ~ 0.8 μm. The results indicate that the common effect of rGO and Fe co-introduction on reducing particle size is more

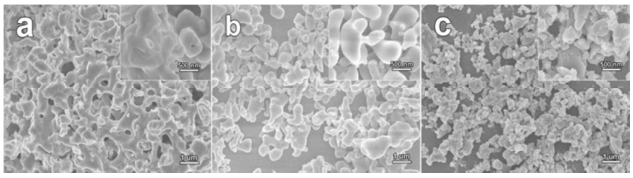


**Figure 4.** SEM images of (a) pristine LVP/C, (b) LVP/C@G3, and (c) LVFP/C@G3-2, respectively.

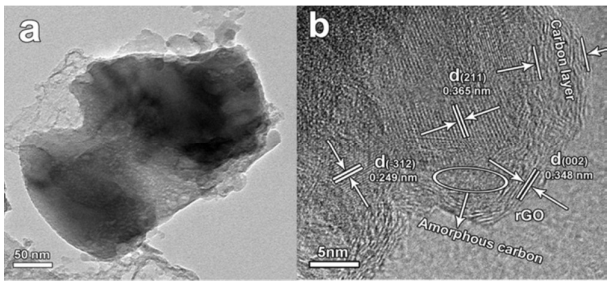


**Figure 5.** TEM images of LVFP/C@G3-2.

obvious than that of single rGO-incorporation. Two things account for this particle size difference: the one is that rGO serves as a surfactant preventing the aggregation of LVP particles during sintering process [47-49]; the other is that cation-doping is beneficial for nucleation process and thus reduce the LVP particle size [42,50]. Especially, under the common effect of rGO-incorporation and cation-doping, the decrease of particle size becomes more obvious [51]. For this reason, LVFP/C@G3-2 powders show the smallest particle size, while LVP/C is just the opposite.

The structure and morphology of LVFP/C@G3-2 powders were further confirmed by TEM (Figure 5). Figure 5a shows that the particle size of LVFP/C@G3-2 is about 500 nm, and the LVFP particle is wrapped or coated by carbon layer. Figure 5b exhibits the high-resolution transmission electron microscope (HRTEM) image of LVFP/C@G3-2. The HRTEM image shows the lattice spacing of d = 0.249 nm and 0.365 nm, corresponding to the (-312) and (211) planes of $P2_1/n$-LVP crystals, respectively. From Figure 5b, it can be also clearly seen that the LVFP/C@G3-2 sample presents a typical core-shell structure with amorphous carbon and rGO wrapping or connecting the LVP particles. The carbon layer with 3 ~ 8 nm thickness is favorable for improving conductivity as well as alleviating vanadium dissolution into the electrolyte [42].

In order to verify Fe-doping, another precise XRD analysis was undertaken for LVP/C, LVP/C@G3 and LVFP/C@G3-2, and Rietveld refinements were performed on the XRD data by using the software Maud to obtain the crystal structure parameters. Figure 6 and Table 2 show the refinement results for LVP/C, LVP/C@G3 and LVFP/C@G3-2, respectively. In Figure 6, the experimental data is represented by the red dots in the figures and the calculated profiles are indicated by the

**Table 2.** Structural parameters of LVP/C, LVP/C@G3 and LVFP/C@G3-2 obtained from XRD Rietveld refinement.

| Sample | *a* (Å) | *b* (Å) | *c* (Å) | Volume (Å$^3$) | $R_w$ (%) | Sig |
|---|---|---|---|---|---|---|
| LVP/C | 8.6065 | 8.6158 | 12.0601 | 894.28 | 10.23 | 0.7921 |
| LVP/C@G3 | 8.6069 | 8.6161 | 12.0603 | 894.37 | 10.56 | 0.7927 |
| LVFP/C@G3-2 | 8.6108 | 8.6095 | 12.0528 | 893.53 | 10.05 | 0.7869 |

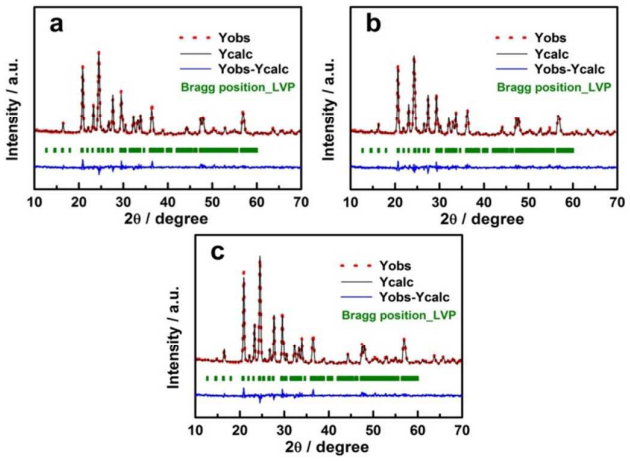


**Figure 6.** Rietveld refinement XRD profiles for (a) LVP/C, (b) LVP/C@G3, and (c) LVFP/C@G3-2.

black lines; the Bragg positions are expressed in the green columns; the difference between the observed and calculated intensity is shown at the bottom of the curves. Table 2 lists the structural parameters of LVP/C, LVP/C@G3 and LVFP/C@G3-2. Obviously, the resulted reliability factors ($R_w$ < 15, Sig < 2) is satisfactory and acceptable. As seen in Table 2, LVP/C@G3 behaves a similar unit cell volume as LVP/C; but LVFP/C@G3-2 presents smaller unit cell volume than LVP/C, which is indicative of Fe-doping. The decreased unit cell volume can be explained by the substitution of Fe ions (0.075 nm for $Fe^{2+}$, or 0.069 nm for $Fe^{3+}$) for $V^{3+}$ (0.078 nm), which agrees well with the previous report [52].

To analyze the effect of rGO-incorporating and Fe-dping on the electrochemical performance of LVP/C, the constant charge/discharge tests at 1 C were carried out. Figs. $7a_1$ and $7b_1$ show the initial charge/discharge curves of LVP/C, rGO modified LVP/C composites (LVP/C@G1, LVP/C@G3 and LVP/C@G5), and Fe-doped composites (LVFP/C@G3-1, LVFP/C@G3-2 and LVFP/C@G3-3). Obviously, all the composites show similar charge/discharge profiles, including four charge plateaus during charge process and an S-shaped curve and two subsequent plateaus during discharge process. The four charge plateaus around 3.69, 3.70, 4.10, and 4.55 V correspond to the four $Li^+$ ions extraction steps from

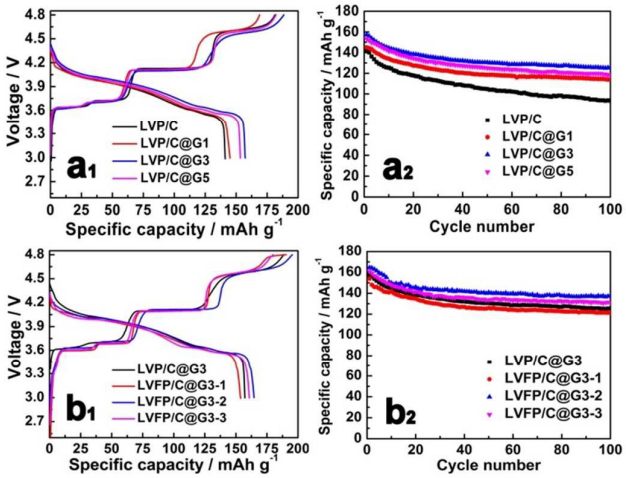


**Figure 7.** (a1, b1) The initial charge/discharge curves, and (a2, b2) the cycle performance of the prepared samples.

**Table 3.** Discharge capacity and capacity retention ratio of the as-prepared samples.

| Sample | Discharge capacity (mAh g-1) | | Capacity retention ratio (%) |
|---|---|---|---|
| | 1$^{st}$ | 100$^{th}$ | 100$^{th}$ to 1$^{st}$ |
| LVP/C | 141.2 | 93.5 | 66.2 |
| LVP/C@G1 | 145.0 | 114.0 | 78.6 |
| LVP/C@G3 | 157.3 | 125.3 | 79.7 |
| LVP/C@G5 | 153.4 | 118.6 | 77.3 |
| LVFP/C@G3-1 | 153.9 | 121.2 | 78.8 |
| LVFP/C@G3-2 | 164.6 | 137.4 | 83.5 |
| LVFP/C@G3-3 | 160.9 | 131.2 | 81.5 |

$Li_3V_2(PO_4)_3$ (i.e., $Li_3V_2(PO_4)_3 \rightarrow Li_{2.5}V_2(PO_4)_3 \rightarrow Li_2V_2(PO_4)_3 \rightarrow LiV_2(PO_4)_3 \rightarrow V_2(PO_4)_3$), the S-shaped curve is ascribed to a solid solution behavior, and the two subsequent plateaus around 3.65 V and 3.58 V is related to a two-phase reaction ($Li_2V_2(PO_4)_3 \rightarrow Li_{2.5}V_2(PO_4)_3 \rightarrow Li_3V_2(PO_4)_3$). As shown in Figure $7a_1$ and Table 3, the initial discharge capacity of LVP/C@G3 is 157.3 mAh $g^{-1}$, which is higher than those of LVP/C (141.2 mAh $g^{-1}$), LVP/C@G1 (145.0 mAh $g^{-1}$) and LVP/C@G5 (153.4 mAh $g^{-1}$). In addition, for LVP/C@G3, the charge plateau shifts downward, the S-shaped curve and discharge plateau shift upward, which is indicative of less polarization for LVP/C@G3 electrode. Figure $7a_2$ shows the corresponding cycle performance profiles. Even after 100 cycles, all the rGO-modified LVP/C samples exhibit much higher capacity than

LVP/C (i.e., 114.0 mAh $g^{-1}$ for LVP/C@G1, 125.3 mAh $g^{-1}$ for LVP/C@G3, 118.6 mAh $g^{-1}$ for LVP/C@G5, but only 93.5 mAh $g^{-1}$ for LVP/C), and also present higher capacity retention ratio than LVP/C (i.e., 78.6 % for LVP/C@G1, 79.7 % for LVP/C@G3, and 77.3 % for LVP/C@G5, but only 66.2 % for LVP/C). Obviously, rGO-incorporation can effectively increase the discharge capacity and cycle stability of LVP/C. Considering that LVP/C@G3 shows the best discharge specific capacity and cycle stability, 3 wt.% GO was used to prepare the Fe-doped composites. Figure 7b shows the initial charge/discharge curves and cycle performance profiles of LVP/C@G3, LVFP/C@G3-1, LVFP/C@G3-2 and LVFP/C@G3-3 composites. It can be clearly seen from Table 3, all the Fe-doped LVP/C@G3 samples exhibit higher initial discharge capacity and capacity retention ratio after 100 cycles than LVP/C@G3. Obviously, Fe-doping can further improve the discharge capacity and cycle stability of LVP/C@G3, especially at an appropriate doping amount ($x$ = 0.06). For comparison, the electrochemical performance of LVP/C, LVP/C@G3 and LVFP/C@G3-2 is presented together in Figure 8 and Table 3. As seen in Figure 8, the charge profile of LVFP/C@G3-2 shifts downward, and the corresponding discharge profile upward, indicative of less polarization for LVFP/C@G3-2. As a result, LVFP/C@G3-2 behaves higher initial discharge capacity and capacity retention ratio (164.6 mAh $g^{-1}$, 83.5 %) than LVP/C@G3 (157.3 mAh $g^{-1}$, 79.7 %) and LVP/C (141.2 mAh $g^{-1}$, 66.2 %).

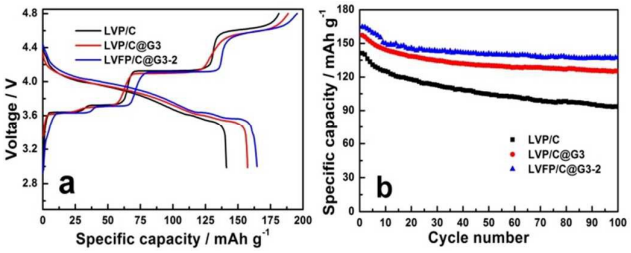


**Figure 8.** Comparison of electrochemical performance between LVP/C, LVP/C@G3 and LVFP/C@G3-2 electrodes.

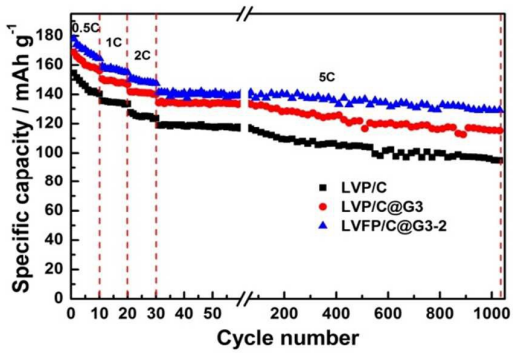


**Figure 9.** Rate performance of LVP/C, LVP/C@G3 and LVFP/C@G3-2 electrodes.

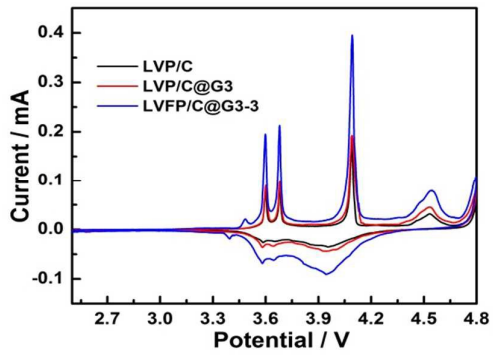


**Figure 10.** CV curves of LVP/C, LVP/C@G3 and LVFP/C@G3-2 electrodes.

Figure 9 and Table 4 further present the rate performance of LVP/C, LVP/C@G3 and LVFP/C@G3-2. It can be seen that with increasing C-rate, the discharge capacity decreases. Nevertheless, after 1030 cycles (first 30 cycles from 0.5 to 2 C every other 10 cycles, then another 1000 cycles at 5 C), LVFP/C@G3-2 even delivers a prominent capacity of 129.3 mAh $g^{-1}$ with a satisfactory capacity retention ratio of 91.5 % (compared to 31$^{st}$ cycle), which means the capacity fading is only 0.0085 % per cycle. The significantly enhanced rate performance is attributed to the common effect of rGO-incorporating and Fe-doping. On the one hand, Fe-doping can enhance structural stability, cause crystal defects, reduce particle size, and decrease charge transfer resistance [53-55]; on the other hand, rGO-incorporation can form more efficiently hybrid conductive network with amorphous carbon, leading to an enhanced electronic conductivity [56-58].

In order to understand the chemical reaction occurring in each sample during charge/discharge process, CV tests were implemented at a slow scanning rate of 0.05 mV $s^{-1}$ over a

**Table 4.** Rate performance of the samples at different charge/discharge rates.

| Sample | 0.5 C | | 1 C | | 2 C | | 5 C | |
|---|---|---|---|---|---|---|---|---|
| | 1$^{st}$ | 10$^{th}$ | 11$^{th}$ | 20$^{th}$ | 21$^{st}$ | 30$^{th}$ | 31$^{st}$ | 1030$^{th}$ |
| LVP/C | 154.6 | 140.3 | 135.6 | 133.5 | 127.7 | 123.7 | 118.9 | 94.9 |
| LVP/C@G3 | 168.8 | 156.2 | 150.5 | 146.8 | 141.7 | 140.0 | 134.3 | 115.3 |
| LVFP/C@G3-2 | 177.8 | 164.5 | 159.1 | 154.8 | 150.3 | 147.6 | 141.3 | 129.3 |

voltage range between 2.5 and 4.8 V. Considering the electrolyte penetration into the electrode, structural change and solid electrolyte interface (SEI) film formation, the second cycle was used to analysis [59]. Figure 10 shows the CV curves of LVP/C, LVP/C@G3 and LVFP/C@G3-2 electrodes. All the electrodes have similar CV curves, including four oxidation peaks around 3.64, 3.73, 4.13 and 4.57 V and three reduction peaks around 3.94, 3.62, 3.55 V. These four oxidation peaks correspond to the extraction of three lithium ions from LVP in a sequence of phase transitions between the single $Li_xV_2(PO_4)_3$ phases ($x$ = 3.0, 2.5, 2.0, 1.0, and 0) [4]. The wide reduction peaks around 3.94 V are related to a solid state behavior: $V_2(PO_4)_3 \rightarrow Li_2V_2(PO_4)_3$, and another two reduction peaks around 3.62 V and 3.55 V correspond to a two-phase transition: $Li_2V_2(PO_4)_3 \rightarrow Li_{2.5}V_2(PO_4)_3 \rightarrow Li_3V_2(PO_4)_3$. The extraction/reinsertion of $Li^+$ ions is associated with the $V^{3+}/V^{4+}$ and $V^{4+}/V^{5+}$ redox couples [11, 60]. It is worth noting that, besides the above-mentioned characteristic redox peaks of LVP, the LVFP/C@G3-2 electrode has another redox peaks around 3.47/3.41 V, which is characteristic of the electrochemical reactions of the $Fe^{2+}/Fe^{3+}$ redox couple in $LiFePO_4$. Compared with LVP/C and LVP/C@G3, LVFP/C@G3-2 shows not only well-defined peaks and the strongest peaks, but also the smallest voltage difference between redox peaks, indicating faster lithium ion diffusion and better reversibility of $Li^+$ ions extraction/reinsertion process.

Figure 11a shows the electrochemical impedance spectroscopies (EIS) for the LVP/C, LVP/C@G3 and LVFP/C@G3-2 fresh cells at open-circuit potential, and all the EIS curves can be fitted by an equivalent circuit composed of "*R(C(RW))*" using the ZSimpWin program [61-63]. All EIS spectra consist of a small intercept at the high frequency, a depressed semicircle at the medium frequency, and a sloping line at the low frequency. The small intercept at high frequency corresponds to the solution resistance of cell ($R_c$); the depressed semicircle at medium frequency is attributed to the charge-transfer resistance at electrode/electrolyte interface ($R_{ct}$) and the double-layer capacitance between electrolyte and cathode ($C_{dl}$); the inclined line at low frequency is attributed to a Warburg impedance related to the diffusion of lithium ions within electrode ($Z_w$). As shown in Figure 11a and Table 1, LVFP/C@G3-2 exhibits a more greatly decreased charge-transfer resistance (20.57 Ω) than LVP/C (54.66 Ω) and LVP/C@G3 (32.51 Ω), indicative of faster kinetics of cell reaction. The lower the charge-transfer resistance, the higher the electrochemical performance [42]. Furthermore, the straight line at low frequency range is associated with lithium ion diffusion in LVP, and the lithium ion diffusion coefficient can be calculated from a straight line at low frequency region according to the following equation [64,65]:

$$D_{Li+} = R^2T^2/2A^2n^4F^4C^2\delta^2$$

where R is the gas constant, T is the absolute temperature, $A$ is the surface area of the cathode, $n$ is the number of electrons per molecule during oxidation, F is the Faraday constant, $C$ is the concentration of lithium ion, and $\delta$ is the Warburg coefficient which is relative with $Z'$ [64,65]:

$$Z' = R_e + R_{ct} + \delta\omega^{-1/2}$$

where $\omega$ is frequency at low frequency region. To obtain the Warburg coefficient ($\delta$), the $Z'$-$\omega^{-1/2}$ relation curves of LVP/C, LVP/C@G3, and LVFP/C@G3-2 are shown in Figure 11b and Table 1. It can be clearly seen that LVP/C and LVP/C@G3 show lithium ion diffusion coefficients of $5.56\times10^{-13}$ $cm^2$ $s^{-1}$ and $2.13\times10^{-12}$ $cm^2$ $s^{-1}$, respectively, while LVFP/C@G3-2 shows the highest lithium ion diffusion coefficient of $2.10\times10^{-11}$ $cm^2$ $s^{-1}$, which accounts for the best electrochemical performance of LVFP/C@G3-2.

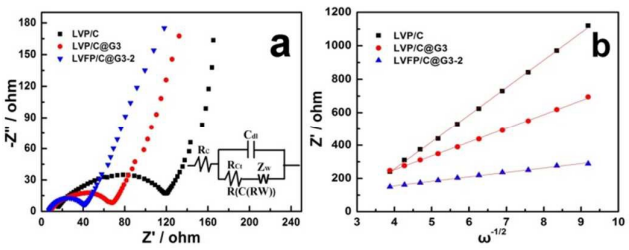


**Figure 11.** (a) EIS spectra, and (b) the relationship between the $Z'$ and $\omega^{-1/2}$ at low frequency of LVP/C, LVP/C@G3 and LVFP/C@G3-2 electrodes.

## 4. Conclusions

In summary, the LVP/C, rGO incorporated LVP/C and rGO incorporated LVFP/C composites were successfully synthesized by sol-gel method and their physicochemical properties and electrochemical performances were studied by XRD, Raman spectroscopy, SEM, TEM, galvanostatic charge/discharge, CV and EIS measurements. The results show that rGO can form an effectively hybrid conductive network with amorphous carbon and enhance the electronic conductivity, meanwhile rGO can reduce the particle size and shorten the transport path of $Li^+$ ions and electrons in LVP. XRD results reveals that $Fe^{2+}$ can enter into the lattice of LVP and exist in the form of $LiFePO_4$. When the rGO-incorporation concentration is 3 wt.% and the Fe-doping dose is 6 at.%, the obtained composite shows the best electrochemical performance with an initial capacity as high as 164 mAh $g^{-1}$ at 1 C, and a prominent capacity of 129.3 mAh $g^{-1}$ even after 1030 cycles at higher rates. The superior rate performance makes Fe-doped and rGO-incorporated $Li_3V_2(PO_4)_3$ a promising cathode candidate for lithium ion batteries. This novel co-modification with Fe-doping and rGO-incorporating can also be easily extended to any other polyanion cathode materials.

## Acknowledgements

This work was supported by the National Science Foundation of China (51302153, 51572151, 51272128) and the Opening

Project of CAS Key Laboratory of Materials for Energy Conversion (CKEM131404).

## Notes and references


1 C. Delacourt, P. Poizot, M. Morcrette, J.M. Tarascon and C. Masquelier, *Chem. Mater.*, 2014, **16**, 93-99.
2 X.L. Wu, L.Y. Jiang, F.F. Cao and Y.G. Guo, *Adv. Mater.*, 2009, **21**, 2710-2714.
3 M.M. Ren, Z. Zhou, X.P. Gao, W.X. Peng and J.P. Wei, *J. Power Sources*, 2006, **162**, 1357-1362.
4 M.Y. Saïdi, J. Barker, H. Huang, J.L. Swoyer and G. Adamson, *J. Power Sources*, 2003, **119**, 266-272.
5 X.H. Rui, N. Yesibolati and C.H. Chen, *J. Power Sources*, 2011, **196**, 2279-2282.
6 H. Huang, S.C. Yin, T. Kerr, N. Taylor and L.F. Nazar, *Adv. Mater.*, 2002, **14**, 1525-1528.
7 C.C. Yang, S.H. Kung, S.J. Lin and W.C. Chien, *J. Power Sources*, 2014, **251**, 296-304.
8 W. Yuan, J. Yan, Z.Y. Tang and L. Ma, *Ionics*, 2012, **18**, 329-335.
9 S.C. Yin, P.S. Strobel, H. Grondey and L.F. Nazar, *Chem. Mater.*, 2004, **16**, 1456-1465.
10 X.Y. Du, W. He, X.D. Zhang, Y.Z. Yue, H. Liu, X.G. Zhang, D.D. Min, X.X. Ge and Y. Du, *J. Mater. Chem.*, 2012, **22**, 5960-5969.
11 M.Y. Saïdi, J. Barker, H. Huang, J.L. Swoyer and G. Adamson, *Electrochem. Solid-State Lett.*, 2002, **5**, A149-A151.
12 X.H. Rui, C. Li and C.H. Chen, *Electrochim. Acta*, 2009, **54**, 3374-3380.
13 W.F. Mao, J. Yan, H. Xie, Z.Y. Tang and Q. Xu, *J. Power Sources*, 2013, **237**, 167-171.
14 A.P. Tang, X.Y. Wang, S.Y. Yang and J.Q. Cao, *J. Appl. Electrochem.*, 2008, **38**, 1453-1457.
15 Y.Z. Li, Z. Zhou, X.P. Gao and J. Yan, *Electrochim. Acta*, 2007, **52**, 4922-4926.
16 H.C. Shin, W.I. Cho and H. Jang, *Electrochim. Acta*, 2006, **52**, 1472-1476.
17 Z.X. Chi, W. Zhang, F.Q. Cheng, J.T. Chen, A.M. Cao and L.J. Wan, *RSC Adv.*, 2014, **4**, 7795-7798.
18 X.F. Zhou, F. Wang, Y.M. Zhu and Z.P. Liu, *J. Mater. Chem.*, 2011, **21**, 3353-3358.
19 Z. Wang, H. Guo and P. Yan, *Electrochim. Acta*, 2015, **174**, 26-32.
20 H.D. Liu, P. Gao, J.H. Fang and G. Yang, *Chem. Commun.*, 2011, **47**, 9110-9112.
21 H. Zhu, X.Z. Wu, L. Zan and Y.X. Zhang, *Electrochim. Acta*, 2014, **117**, 34-40.
22 G. Jo, M. Choe, S. Lee, W. Park, Y. H. Kahng and T. Lee, *Nanotechnology*, 2012, **23**, 112001-112020.
23 I. Meric, M.Y. Han, A.F. Young, B. Ozyilmaz, P. Kim and K.L. Shepard, *Nat. Nanotechnol.*, 2008, **3**, 654-659.
24 J.H. Chen, C. Jang, S.D. Xiao, M. Ishigami and M.S. Fuhrer, *Nat. Nanotechnol.*, 2008, **3**, 206-209.
25 C. Lee, X.D. Wei, J.W. Kysar and J. Hone, *Science*, 2008, **321**, 385-389.
26 D.V. Kosynkin, A.L. Higginbotham, A. Sinitskii, J.R. Lomeda, A. Dimiev, B.K. Price and J.M. Tour, *Nature*, 2009, **458**, 872-877.
27 C. Wang, K. Su, W. Wan, H. Guo, H.H. Zhou, J.T. Chen, X.X. Zhang and Y.H. Huang, *J. Mater. Chem. A*, 2014, **2**, 5018-5023.
28 X.W. Wang, Z.A. Zhang, Y.H. Qu, Y.Q. Lai and J. Li, *J. Power Sources*, 2014, **256**, 361-368.
29 Y.L. Ruan, K. Wang, S.D. Song, X. Han and B.W. Cheng, *Electrochim. Acta*, 2015, **160**, 330-336.
30 Z.S. Feng, C. Zhang, J.J. Chen, Y. Wang, X. Jin, R. Zhang and J. Hu, *RSC Adv.*, 2013, **3** 4408-4415.
31 Y. Li, D. Xie, Y.D. Zhang, D. Zhou, X.Q. Niu, Y.Y. Tong, D.H. Wang, X.L. Wang, C.D. Gu and J.P. Tu, *J. Mater. Chem. A*, 2015, **3**, 14731-14740.
32 L.L. Zhang, S. Duan, X.L. Yang, G. Peng, G. Liang, Y.H. Huang, Y. Jiang, S.B. Ni and M. Li, *ACS Appl. Mater. Interfaces*, 2013, **5**, 12304-12309.
33 Y. Huang, H. Liu, Y.C. Lu, Y.L. Hou and Q. Li, *J. Power Sources*, 2015, **284**, 236-244.
34 B. Wang, W.A. Abdulla, D.L. Wang and X.S. Zhao, *Energy Environ. Sci.*, 2015, **8**, 869-875.
35 Y.H. Chen, Y.M. Zhao, X.N. An, J.M. Liu, Y.Z. Dong and L. Chen, *Electrochim. Acta*, 2009, **54**, 5844-5850.
36 T. Jiang, Y.J. Wei, W.C. Pan, Z. Li, X. Ming, G. Chen and C.Z. Wang, *J. Alloys Comp.*, 2009, **488**, L26-L29.
37 L.L. Zhang, G. Liang, G. Peng, Y. Jiang, H. Fang, Y.H. Huang, M.C. Croftd and A. Ignatov, *Electrochim. Acta*, 2013, **108**, 182-190.
38 S.Q. Liu, S.C. Li, K.L. Huang and Z.H. Chen, *Acta Phys. -Chim. Sin.*, 2007, **23**, 537-542.
39 S.K. Zhong, L.T. Liu, J.Q. Jiang, Y.W. Li, J. Wang, J.Q. Liu and Y.H. Li, *J. Rare Earths*, 2009, **27**, 134-137.
40 C.S. Dai, Z.Y. Chen, H.Z. Jin and X.G. Hu, *J. Power Sources*, 2010, **195**, 5775-5779.
41 J.X. Dang, F. Xiang, N.Y. Gu, R.B. Zhang, R. Mukherjee, I.K. Oh, N. Koratkar and Z.Y. Yang, *J. Power Sources*, 2013, **243**, 33-39.
42 L.L. Zhang, G. Liang, G. Peng, Y.H. Huang, L. Wang, L. Qie, M.C. Croft, A. Ignatov and J.B. Goodenough, *J. Electrochem. Soc.*, 2012, **159**, A1573-A1578.
43 Z.Y. Wang, M.A. Fierke and A. Stein, *J. Electrochem. Soc.*, 2008, **155**, A658-A663.
44 O.P. Krivoruchko, N.I. Maksimova, V.I. Zaikovskii and A.N. Salanov, Carbon, 2000, **38**, 1075-1082.
45 P.C. Li, Nature, 1961, **192**, 864-865.
46 H. Marsh, D. Crawford and D.W. Taylor, Carbon, 1983, **21**, 81-87.
47 B. Pei, Z. Jiang, W. Zhang, Z. Yang and A. Manthiram, J. Power Sources, 2013, **239**, 475-482.
48 X. Zhu, Z. Yan, W. Wu, W. Zeng, Y. Du, Y. Zhong, H. Zhai, H. Ji and Y. Zhu. Sci. Rep., 2014, **4**, 5768-5775.
49 M.S. Choi, H.S. Kim, Y.M. Lee and B.S. Jin, J. Mater. Chem. A, 2014, **2**, 7873-7879.
50 H. Shu, X. Wang, W. Wen, Q. Liang, X. Yang, Q. Wei, B. Hu, L. Liu, X. Liu, Y. Song, M. Zho, Y. Bai, L. Jiang, M. Chen, S. Yang, J. Tan, Y. Liao and H. Jiang, Electrochim. Acta, 2013, 89, 479-487.
51 M. Choi, H.S. Kim, Y.M. Lee, W.K. Choi and B.S. Jin, Mater. Lett., 2015, **160**, 194-199.
52 L.L. Zhang, S. Duan, G. Peng, G. Liang, F. Zou and Y.H. Huang, *J. Alloys Comp.*, 2013, **570**, 61-64.
53 L. Liu, J.D. Chen, Y.J. Bai, L. Fang, H.J. Zhang and Y. Wang, *J. Mater. Chem. A*, 2015, **3**, 6671-6678.
54 H.H. Yi, C.L. Hu, X.M. He and H.Y. Xu, *Ionics*, 2015, **21**, 667-671.
55 D.D. Lecce, J. Manzi, F.M. Vitucci, A.D. Bonis, S. Panero and S. Brutti, *Electrochim. Acta*, 2015, **185**, 17-27.
56 H.K. Roh, H.K. Kim, K.C. Roh and K.B. Kim, *RSC Adv.*, 2014, **4**, 31672-31677.
57 S. Monaco, F.D. Giorgio, L.D. Col, M. Riché, C. Arbizzani and M. Mastragostino, *J. Power Sources*, 2015, **278**, 733-740.
58 J.Y. Mun, H.W. Ha and W. Choi, *J. Power Sources*, 2014, **251**, 386-392.
59 X.C. Zhou, Y.M. Liu and Y.L. Guo, *Electrochim. Acta*, 2009, **54**, 2253-2258.
60 L.J. Wang, X.C. Zhou and Y.L. Guo, *J. Power Sources*, 2010, **195**, 2844-2850.
61 L.L. Zhang, G. Liang, G. Peng, F. Zou, Y.H. Huang, M.C. Croft and A. Ignatov, *J. Mater. Chem. C*, 2012, **116**, 12401-12408.

62 W. Xu, L. Liu, H. Guo, R. Guo and C. Wang, Electrochim. Acta, 2013, **113**, 497-504.
63 W.F. Mao, Y.B. Fu, H. Zhao, G. Ai, Y.L. Dai, D.C. Meng, X.H. zhang, D.Y. Qu, G. Liu, V.S. Battaglia and Z.Y. Tang, ACS Appl. Mater. Interfaces, 2015, **7**, 12057-12066.
64 C. Wei, W. He, X. Zhang, S. Liu, C. Jin, S. Liu and Z. Huang. RSC Adv., 2015, **5**, 28662-28669.
65 X. Du, W. He, X. Zhang, Y. Yue, H. Liu, X. Zhang, D. Min, X. Ge and Y. Du, J. Mater. Chem., 2012, 22, 5960-5969.